Oriented Growth of α-MnO₂ Nanorods Using Natural Extracts from Grape Stems and Apple Peels

Lina Sanchez-Botero [1], Adriana P. Herrera [2] and Juan P. Hinestroza [1],*

[1] Department of Fiber Science and Apparel Design, Cornell University, Ithaca, NY 14853, USA; lms374@cornell.edu
[2] Department of Chemical Engineering, Universidad de Cartagena, Cartagena 130015, Colombia; aherrerab2@unicartagena.edu.co
*   Correspondence: jh433@cornell.edu; Tel.: +1-607-255-7600

Abstract: We report on the synthesis of alpha manganese dioxide (α-MnO₂) nanorods using natural extracts from *Vitis vinifera* grape stems and *Malus domestica* 'Cortland' apple peels. We used a two-step method to produce highly crystalline α-MnO₂ nanorods: (1) reduction of KMnO₄ in the presence of natural extracts to initiate the nucleation process; and (2) a thermal treatment to enable further solid-state growth of the nuclei. Transmission electron microscopy (TEM) and field emission scanning electron microscopy (FESEM) images provided direct evidence of the morphology of the nanorods and these images were used to propose nucleation and growth mechanisms. We found that the α-MnO₂ nanorods synthesized using natural extracts exhibit structural and magnetic properties similar to those of nanoparticles synthesized via traditional chemical routes. Furthermore, Fourier transform infrared (FTIR) shows that the particle growth of the α-MnO₂ nanorods appears to be controlled by the presence of natural capping agents during the thermal treatment. We also evaluated the catalytic activity of the nanorods in the degradation of aqueous solutions of indigo carmine dye, highlighting the potential use of these materials to clean dye-polluted water.

Keywords: nanorods; manganese oxide; natural extracts; dye degradation; oriented attachment; green synthesis

1. Introduction

During the past decade, the synthesis of anisotropic metal oxide nanoparticles has attracted considerable attention because of their unique size- and shape-dependent properties [1–3]. Self-assembly processes driven by diverse interactions can generate a myriad of nanostructures by using nanocrystals as building blocks. Shape control of these structures can be achieved by tuning some of the synthesis parameters such as temperature, type of ligands, and interaction of the ligands with the precursors and/or the nanoparticles [4–6]. This means that the thermodynamics and kinetics of nucleation and growth can also be controlled [7,8]. Among the variety of possible shapes, nanorods are some of the most studied anisotropic materials as the combination of chemically induced growth and shape anisotropy can offer an additional level of control during self-assembly processes driven by structural and chemical selectivity [9,10].

Although many approaches have been followed for the synthesis of nanomaterials, the need to minimize toxic reagents, and to develop green synthesis processes that yield nanomaterials with similar properties to those synthesized using traditional methods remain a valid one [11]. Methods for the synthesis of nanoparticles using plant and fruit extracts are well-established in the scientific literature and several nanoparticles have been synthesized using natural extracts including gold [12,13], platinum [14], iron oxide [15–17], copper [18,19], palladium [20,21], zinc oxide [22], and silver [23–27].

Few studies have explored the synthesis of manganese oxide nanoparticles using a green synthesis route [28–30]. To our knowledge, there are no studies exploring the use of natural extracts for the oriented growth of highly crystalline alpha manganese dioxide (α-MnO$_2$) nanorods, which is the main topic of this paper.

The synthesis of manganese oxide nanoparticles continues to be an area of active research as these particles can be used in catalysis [31], batteries [32], and supercapacitor applications [33,34]. MnO$_2$ nanoparticles have been synthesized by a variety of techniques and in several shapes such as nanorods [32,33], nanowires [35], whiskers [36], and dandelion-like three dimensional structures [37]. Among the catalytic applications for manganese oxides are the degradation of dyes [38–41], water-oxidizing processes [42], and the photocatalytic oxidation of organic pollutants in waste water [43]. The most commonly used reducing agents include nitric acid (HNO$_3$) [32], sodium hydroxide (NaOH) [33], hydrochloric acid (HCl) [40], and ammonium fluoride (NH$_4$F) [35]. Alternative synthesis methods for manganese oxide particles include hydrothermal processes [44,45], molten salt routes [46], and microemulsion methods [47].

We hereby report a simple approach using natural extracts from apple peels and grape stems, to fabricate α-MnO$_2$ nanorods. We found that the morphological and structural properties of the nanorods produced using these natural extracts are similar to the properties of the nanorods synthesized using traditional methods [32,33,48,49]. We also propose a mechanism to explain the formation of α-MnO$_2$ nanorods. Furthermore, we tested the catalytic activity of the synthesized α-MnO$_2$ nanorods on the degradation of aqueous solutions of indigo carmine dye. Finally, we found that these nanorods are very stable and suitable for repeated use. The synthesis method reported here may be easily extended to a wide variety of other metal oxide nanomaterials.

2. Results and Discussion

2.1. Materials Synthesis and Characterization

Figure 1 shows the X-ray diffraction (XRD) patterns of samples V6 and V8, corresponding to the nanorods synthesized using the *Vitis vinifera* extracts, as well as samples A6 and A8, corresponding to the specimens synthesized with the *Malus domestica* extracts. According to the XRD patterns, the crystallinity of the synthesized products improves with further calcination at 600 °C and 800 °C, and this behavior is consistent with prior observations for the synthesis of α-MnO$_2$ nanocrystals [50–52]. For the as-synthesized powders made with the *Malus domestica* extract (Figure 1a), few diffraction peaks can be observed. In contrast, the as-synthesized powders made with *Vitis vinifera* (Figure 1d) exhibit peaks that can be easily indexed to the potassium manganese oxide KMnO$_2$ phase (Joint Committee on Powder Diffraction Standards-JCPDS, card no.: 044-1025) and MnO$_2$ phase (JCPDS, card no.: 053-0633), as shown in Figure S1a.

After thermal treatment, the crystalline structure of both samples progressively evolves towards α-MnO$_2$ (JCPDS, card no.: 44-0141). XRD patterns in Figure 1b,c synthesized using the *Malus domestica* extract, exhibit a high intensity peak at 37.5°, which can be indexed as the (211) plane followed in intensity by the peaks for the planes (310) and (110). In contrast, for samples synthesized with the *Vitis vinifera* extract, Figure 1e,f, shows that the most dominant peak occurs at a plane (110) and a 2θ value of 12.5° followed by planes (211) and (310). It is important to note that regardless of the natural extract used for the synthesis, the calcinated samples at 800 °C exhibit an increase in the peak intensity and a decrease in peak broadening when compared to the same samples calcinated at 600 °C. Careful comparison of the relative intensities of the dominant diffraction peaks shows that the intensity of the peaks (110) and (220), are higher. Noting that (220) is only a short range of (110), thus, the relative intensity of the (110) peak for sample V-8 (43.2%) and for sample A-8 (100.0%) is much stronger than that shown in the standard JCPDS card (37.0%). Likewise, the relative intensity of the (220) peak for sample V-8 (35.7%) and for sample A-8 (11.62%) are 7.14 and 2.3 times the value stated in the standard JCPDS card. However, the relative intensities of the other diffraction peaks are comparable or smaller

to those intensities reported in the standard JCPDS card. Thus, these results suggest a preferential growth of α-MnO$_2$ in both cases [53]. It is worth noting that the calculated ratio between the intensities of the (211) and (310) diffraction peaks for samples V8 and A8 were slightly lower than that reported in the JCPDS standard (1.1 and 1.04 versus 1.2, respectively). Figure S6 shows the square tunnel structure of α-MnO$_2$ with space group I 4/m, with the dominant planes highlighted by the grey shaded areas. The α-MnO$_2$ structures were plotted using visualization for electronic and structural analysis (VESTA) software [54].

The crystallite size and the lattice parameters, calculated using the XRD patterns, are summarized in Table 1. The basic building block for most of the Mn oxide structures is the MnO$_6$ octahedron, and in the α-MnO$_2$ structure, these octahedra are assembled by sharing edges that form a tunnel structure (as shown in the inset of Figure 1) [55–57].

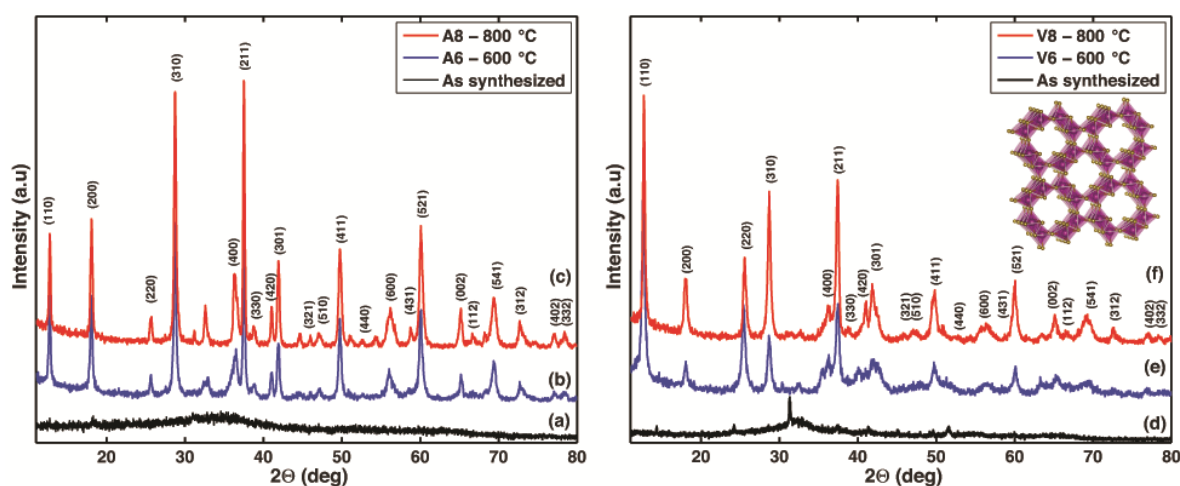**Figure 1.** X-ray diffraction (XRD) patterns of the as-synthesized sample and alpha manganese dioxide (α-MnO) nanoparticles under different calcination temperatures (600 °C, 800 °C). (**a**–**c**) corresponds to experiments using the *Malus domestica* Cortland Apple Peels extract and (**d**–**f**) to experiments using the *Vitis vinifera* Grape stems extract.

Table 1. Crystallite size and the lattice parameters of the α-MnO$_2$ nanorods produced with the *Malus domestica* apple peel extract (A6 and A8) and with the *Vitis vinifera* stems extract (V6 and V8).

Sample Name	Extract Used in the Synthesis	Calcination Temperature (°C)	Crystallite Size (Å)	a (Å)	b (Å)
A6	*Malus domestica*	600	D211: 314	9.892	2.873
A8	*Malus domestica*	800	D211: 352	9.814	2.861
V6	*Vitis vinifera*	600	D110: 243	9.922	2.854
V8	*Vitis vinifera*	800	D110: 356	9.874	2.861

Figure 2a–f shows scanning electron microscope (SEM) and TEM images of samples synthesized with the *Malus domestica* extract. These images show the presence of short and long rods that are dense and agglomerated with diameters ranging from 28 to 70 nm and lengths between 85 and 180 nm. Conversely, in Figure 2g–l, when the *Vitis vinifera* extract was used, larger nanorods were obtained and with a larger aspect ratio. The nanorods synthesized with *Vitis vinifera* do exhibit a wider particle size distribution between 150 and 800 nm in length and from 40 to 80 nm in diameter.

Figure 3a–c shows the FTIR spectra corresponding to the samples prepared with the *Malus domestica* extract, while the spectra displayed in Figure 3d–f correspond to the samples prepared using the *Vitis vinifera* stems extract. The as-synthesized samples exhibited broad peaks around 3600–3000 cm^{-1}, which could be assigned to the –OH stretching and H–O–H bending vibrations of

bound water molecules adsorbed onto the crystalline domains [58]. The peak near 1600–1625 cm^{-1} reveals the involvement of C=O stretching vibration of acid derivatives [16]. In addition, peaks at 2900–2875 cm^{-1} and 1375–1310 cm^{-1} can be related to C–H in-plane bending and aliphatic C–O stretching modes [58]. These peaks are indicative of the presence of organic molecules that originated from the phytochemical components of the natural extracts, i.e., esters and alcohols. The spectra also exhibit peaks at 1060, 875, 850, 630, and 560 cm^{-1}, which can be related to M=O stretching vibration, Mn–O–H bending, MnO$_4^-$ tetrahedral, Mn–O vibrations in octahedral environments, and Mn–O–Mn bonds, which are characteristic bands for manganese oxide [29,30,58].
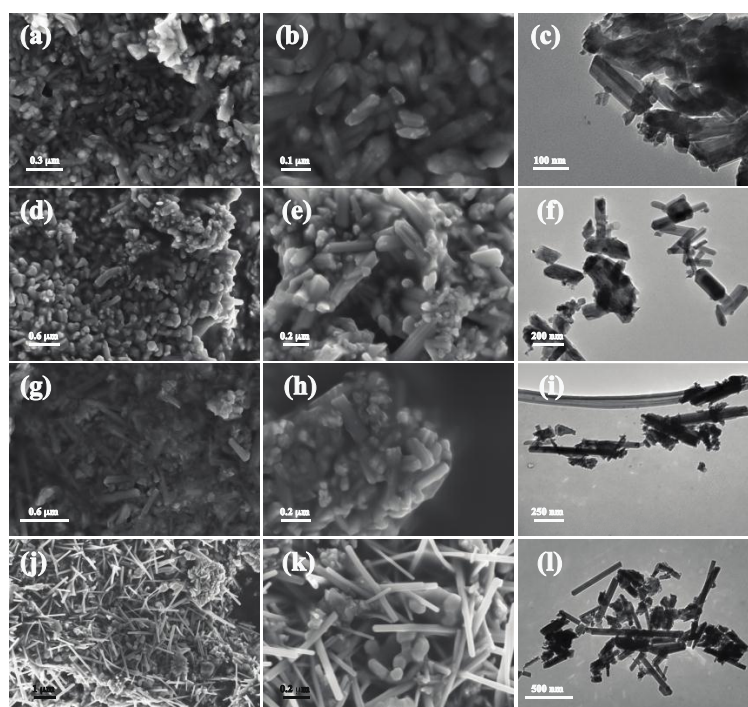

Figure 2. Field emission scanning electron microscopy (FESEM) and transmission electron microscopy (TEM) images of manganese oxide (α-MnO$_2$) nanorods at different magnifications. (**a**–**c**) *Malus domestica* apple peel extract, calcinated at 600 °C; (**d**–**f**) *Malus domestica* apple peel extract, calcinated at 800 °C; (**g**–**i**) *Vitis vinifera* stems extract, calcination at 600 °C; (**j**–**l**) *Vitis vinifera* stems extract, calcinated at 800 °C.
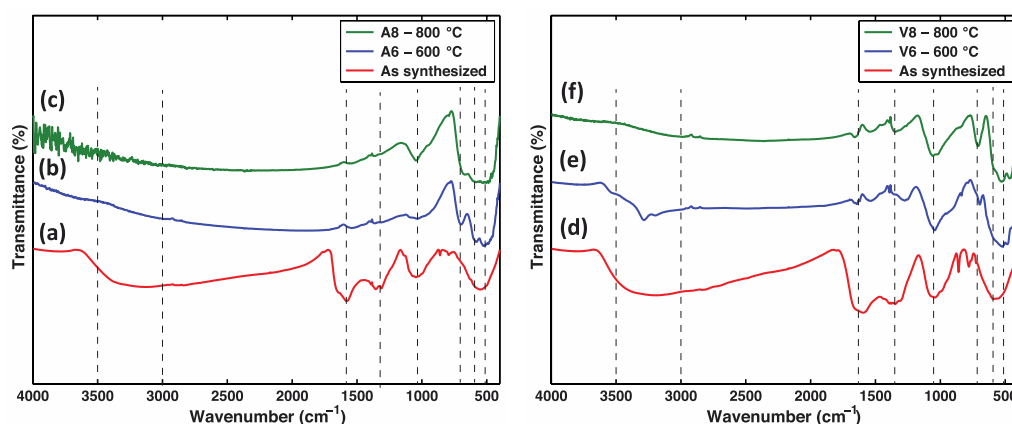

Figure 3. Fourier transform infrared (FTIR) spectrum of Manganese Oxide in the range from 500 to 3800 cm^{-1}, KBr pellet sampling (**a**–**c**) *Vitis vinifera* stems extract; (**d**–**f**) *Malus domestica* apple peels extract.

Upon calcination to 800 °C, changes in the FTIR spectrum can be observed in Figure 3c,f. For example, the absorption bands assigned to the vibrations of the O–H and O–H–O groups of the absorbed water (3600–3000, 2000–1300 cm^{-1}) disappear. In addition, the disappearance of the absorption bands at 1375–1355 cm^{-1} and at 850–875 cm^{-1} could be ascribed to the complete decomposition of the adsorbed phytochemicals after calcination which is confirmed by the thermal analysis presented in Figure S4. As the calcination temperature increases, the intensity of the bands at the frequencies below 750 cm^{-1} increases—these bands are ascribed to the metal-oxygen Mn–O–Mn and Mn–O bending vibrations of the [MnO$_6$] octahedral in α-MnO$_2$. These results are consistent with the XRD analysis reported above and are in quantitative agreement with the results reported in the literature for other MnO$_2$ nanoparticles [32,36,59].

The thermal analysis (TG-DTG) of the as-synthesized products are shown in Figure S4. The thermogram curve and its derivative show two main stages of weight loss. The first stage occurs at about 100 °C and can be attributed to water loss (endothermic peak in the derivative curve). The second stage occurs between 300 and 375 °C and can be related to the burning of residual adsorbed phytochemicals that act as capping agents and the formation of highly crystalline α-MnO$_2$. Above 600 °C, the weight loss is almost negligible.

X-ray photoelectron spectra of the six samples are shown in Figure 4. For all the samples, the binding energy of the C1s level at 284.6 eV was used as an internal reference to calibrate every spectrum to minimize charging effects. The binding energies (BE) of Mn(2p$_{3/2}$) and Mn(2p$_{1/2}$) are summarized in Table 2, and these values are in good accordance with those of the tetravalent manganese system MnO$_2$ [60–63]. However, three samples, the as-synthesized sample with the *Malus domestica* extract, the as-synthesized sample with the *Vitis vinifera* extract, and the sample synthesized with the *Malus domestica* extract and calcinated at 600 °C (A6), all display a small but distinct shoulder at about 3 eV from the main peak. These features are also present in the calculated Mn^{+4} spectrum by Gupta and Sen [64] and Nesbitt and Barnejee [61]. This can be due to the non-stoichiometry nature of MnO$_2$ hence, the occurrence of mixed valence compounds is also likely to be involved in the overall reaction [64,65]. As can be seen in Table 2, the presence of Mn^{+4} in the Mn(2p) spectrum is appreciable in supporting the findings from the XRD experiments. The spectrum O 1 s in Figure S5 reveals three types of the O atom in the as-synthesized samples. The first is assigned as a lattice oxygen Mn–O–Mn (529−530 eV) and dominates in the O1s-line, and the second can be describe as hydrated Mn–O–H manganese oxides (531–532 eV). The third corresponds to the oxygen of the absorbed water H–O–H (533 eV). After calcination, the peak assigned to the presence of lattice oxygen forming the strong Mn–O–Mn bonds in the crystalline network, progressively shifts to 529.9 eV. The intensity of the hydrated Mn–O–H peak decreases as the calcination temperature increases. All of the peak values and their evolution due to calcination are in quantitative agreement with the reported data for α-MnO$_2$ [55,61,63].

Table 2. Mn(2p$_{3/2}$) and Mn(2p$_{1/2}$) spectral fitting and peak binding energy (eV) maxima

Sample	Extract	Temp (°C)	Mn(2p$_{3/2}$) (eV)	Mn(2p$_{3/2}$) (eV), pk 2	Mn(2p$_{1/2}$) (eV)
As-synthesized	*Malus domestica*	–	641.19	643.99	653.26
A6	*Malus domestica*	600	641.75	644.55	653.33
A8	*Malus domestica*	800	640.99	–	652.22
As-synthesized	*Vitis vinifera*	–	642.7	647.1	654.33
V6	*Vitis vinifera*	600	641.92	–	653.28
V8	*Vitis vinifera*	800	641.97	–	653.43

The magnetic properties of the α-MnO$_2$ nanorods were measured using a vibrating sample magnetometer (VSM). Figure 5a,b shows the M–H curves for the α-MnO$_2$ samples at 300 K and 5 K. The M–H curves at 300 K shows no sign of saturation even when the applied fields have a magnitude of 7 kOe. This strong linear response reveals a superparamagnetic state for the α-MnO$_2$ nanorods at this temperature. However, the M–H curves at 5 K show a hysteresis loop and no sign of saturation magnetization. At this temperature, all samples exhibit exchange bias behavior that can be calculated using two fields: the exchange bias field, H$_{EB}$, and the coercive field, H$_C$. H$_C$ = abs(H$_{C1}$ − H$_{C2}$)/2 and H$_{EB}$ = (H$_{C1}$ + H$_{C2}$)/2, where H$_{C1}$ and H$_{C2}$ are the left and right coercive fields, respectively. Samples A6 and A8 exhibit the same coercive field and exchange bias field, 307.15 and −1.35 Oe, respectively, indicating that there is no influence of the calcination temperature on the magnetic properties of these specimens. In contrast, for samples V6 and V8 the coercive field and exchange bias field vary, 127.85 Oe and −15.55 Oe for V6 and 210.25 Oe and −44.05 Oe for V8, respectively. This variation highlights the fact that the calcination temperature, in the *Vitis vinifera* specimens, has an influence on the magnetic properties of the nanorods.

This behavior may be explained on the basis of their different preferential crystalline orientations. The exchange bias effect appears stronger in the samples synthesized with the *Malus domestica* apple peels extract than in the samples obtained with the *Vitis vinifera* grape stem extract [66]. For all samples, the magnetization of the specimens decreases with increasing calcination temperature. Figure 5c,d shows the temperature-dependent magnetization curves measured under the zero-field-cooling (ZFC) and field-cooling (FC) modes from 5 K to 300 K under 100 Oe. The observed Neel temperatures (T$_N$) of the samples are lower than the ones reported for MnO$_2$ bulk crystals (92 K), which is expected for the difference in the crystallite sizes [67]. In Figure 5d, a smaller peak is observed in the ZFC curve at ca. 10 K. This peak can be ascribed to the magnetic blocking of a fraction of smaller rods in the specimen [68,69]. Such magnetic behavior, including superparamagnetic responses, exchange bias field response, and the presence of multimodal blocking temperatures, hint at several interesting prospects for future studies and applications of these nanorods in magnetic nanodevices [70,71].
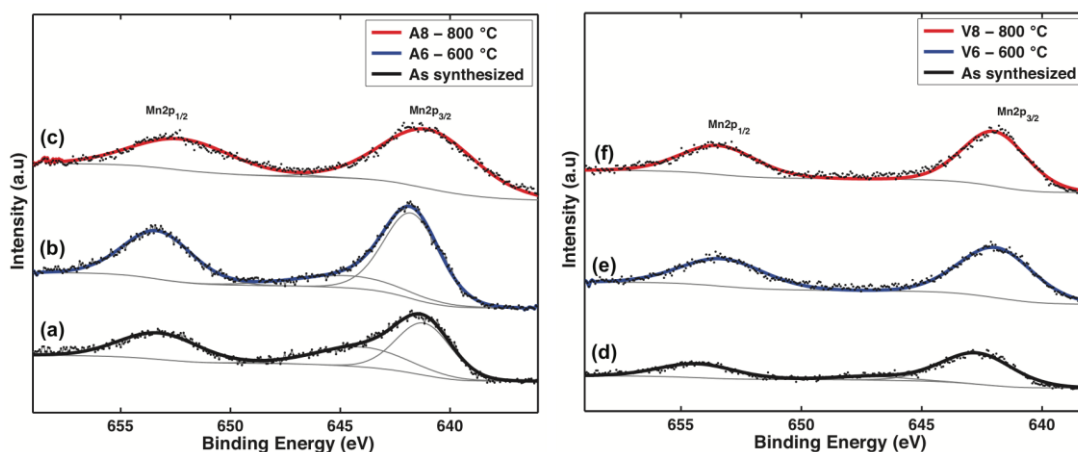

Figure 4. X-ray photoelectron spectroscopy (XPS) Spectra of the Manganese Oxide samples. (**a**–**c**) samples synthesized with the *Vitis vinifera* stems extract; (**d**–**f**) samples synthesized with the *Malus domestica* apple peels extract (BE values are corrected using the carbon peak at 284.6 eV as a reference).
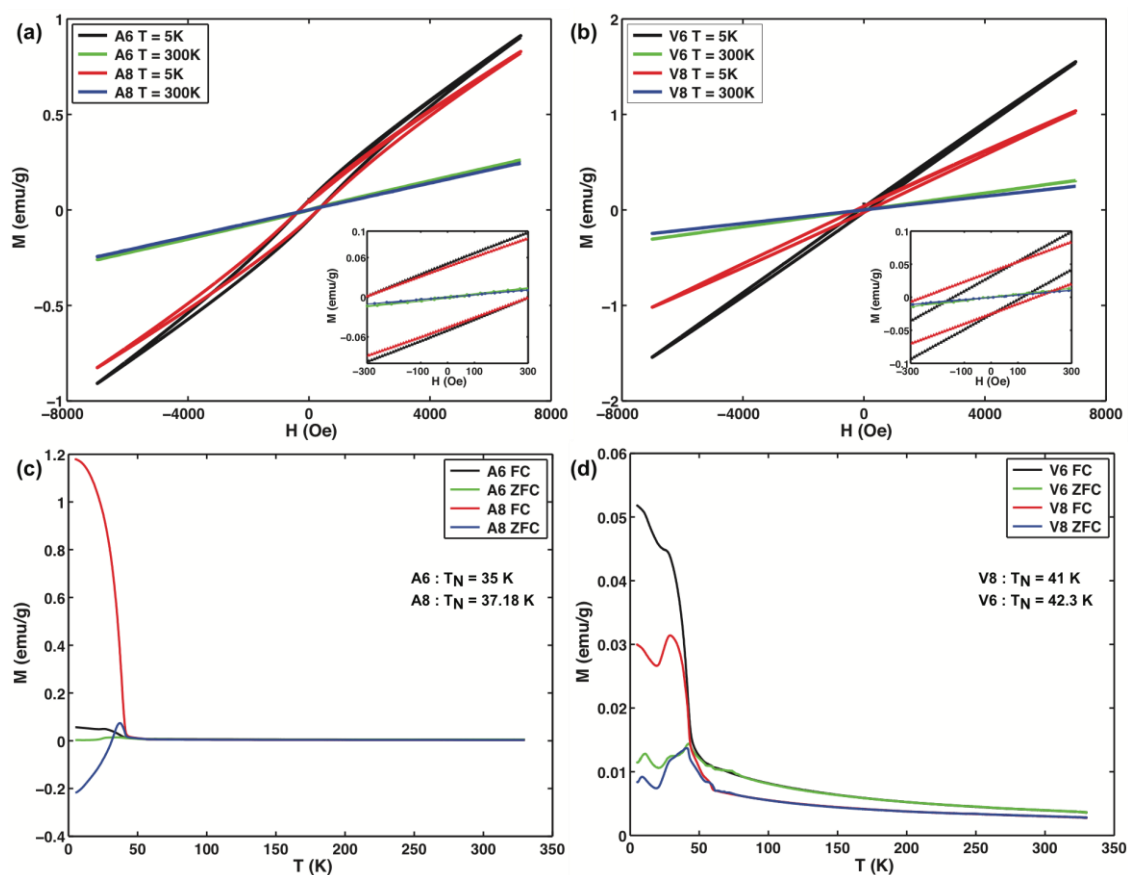
Figure 5. Magnetization as a function of the applied field at 5 K and 300 K for samples (**a**) A6, A8; (**b**) V6, V8; and zero-field-cooling (ZFC)/field cooling (FC) magnetization curves of the α-MnO$_2$ nanorods under an applied field of 100 Oe for samples; (**c**) A6, A8; (**d**) V6, V8.

2.2. Proposed Growth Mechanism

The nature of the natural extracts used in the experiments appear to have a significant morphological effect on the growth of the nanorods. Since all experimental conditions were the same, we believe that the variation of the phytochemical content in the solvent media influences the size of the α-MnO$_2$ nanorods, their crystallite sizes, and their preferential crystal growth direction. A possible explanation for these results is that the phytochemicals act as reducing and stabilizer agents that control the diffusion of growth during the nucleation process [12,23]. We believe that the initial nucleation of the MnO$_2$ nanorods follows the Ostwald ripening process and after nucleation, the nuclei experience a temperature-induced oriented attachment (OA) growth. In this particle-mediated crystal growth mechanism, the individual nanocrystals are integrated and fused into highly anisotropic structures with preferential crystallographic orientations [7,9]. Figure 6 shows the proposed evolution and phase transformation mechanism.

We speculate that the natural stabilizing agents capping the nuclei particles may modulate the oriented attachment (OA) growth during the calcination processes [7,10]. The assembly appears to be driven by the presence of the phytochemicals acting as ligands and selectively binding to specific crystal faces, hence enabling the growth of the manganese oxide nanorods. The proposed mechanism appears to be supported by the XRD, thermal gravimetric analysis (TGA), and FTIR results. However, the exact role of these natural capping agents during the calcination process cannot be fully determined in this study. Figure S1b shows the HRTEM of the as-synthesized sample with *Vitis vinifera*, demonstrating that the nanorods indeed grow from the small nanoparticles. This behavior is similar to that reported by Polleux et al. [72] in which anisotropic TiO$_2$ nanocrystals were synthesized by ligand-directed

assembly of the nanoparticles. Similarly, Tang et al. [73] reported that the removal of excess stabilizer was the key step in the preparation of CdTe nanowires from nanoparticles. Previous studies also show morphological differences in the manganese oxide nanoparticles obtained using different solvents. For example, Yan et al. [28] synthesized Mn_3O_4 nanoparticles using Banana peel extract and obtained agglomerated particles with diameters from 20 to 50 nm. In contrast, Sharma et al. [30] reported the synthesis of Mn_3O_4 nanoparticles using the leaf extract of *Azdirachta indica* and obtained uniform spherical particles with diameters between 20 and 30 nm.
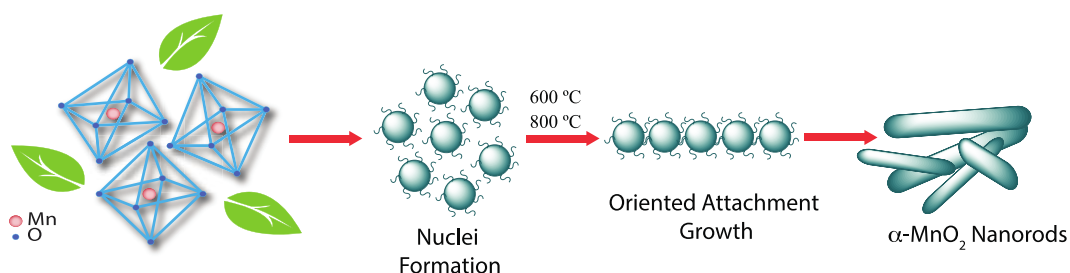

Figure 6. Schematic representation of the proposed nucleation and growth mechanism of α-MnO_2 nanorods using natural extracts from *Malus domestica* and *Vitis vinifera*.

The analysis of the chemical constituents of *Malus domestica* and *Vitis vinifera* extracts was performed via gas chromatography mass spectrometry (GC-MS). Figure S2a,b shows the mass spectra of dominant compounds in each extract and the identified compounds are shown in Tables S1 and S2. For simplicity, we have categorized the main compounds in Table S3 into seven groups: chelating agents, alcohols, ketones, esters, carbohydrates, aldehydes, and others. The presence of chelating agents with COOH groups play a critical role in capping the nanoparticles and may control the growth during the calcination process [72,74]. Aldehydes and ketones have been reported to act as reducing agents in nanoparticle formation processes [75–77]. Additionally, these groups can provide colloidal stability by forming a thin layer on the surface of the nanoparticles [24,78]. Curiously, polyphenols were not detected; this may be due the nature of the solvent used in the extraction method for the GC-MS characterization. The phytochemical constituents in plants are affected by the extraction solvents shown by Abdel-Aal et al., who performed the extraction of *Spirogyra longata algea* with petroleum ether, methylene chloride, chloroform, acetone, and methanol, and found that the extraction solvent influenced the nature of the extracted molecules, especially that of alkaloid phenolics and sterols [79].

2.3. Assesing the Catalytic Activity of the Nanoparticles in Dye Degradation

Figure 7 shows the degradation behavior of a 20 ppm solution of indigo carmine (IC) dye in the presence of the α-MnO_2 nanorods. The degradation of the dye solution was monitored by ultraviolet-visible (UV-Vis) spectrophotometry, using its characteristic absorption at 610 nm. For the degradation studies, we used the optimized conditions reported elsewhere [38]: briefly, the pH of the 20 ppm indigo carmine solution was adjusted to 2.5, by the addition of CH_3COOH, and after pH adjustment, the α-MnO_2 nanorods were added at different concentrations (0.2%, 0.1%, 0.05%, 0.025% *w/v*). The samples were vortexed for 30 s and centrifuged for 15 min at 10,000 rpm. The percentage of degradation was calculated using the following formula: %Degradation = $(A_0 - A_f) \times 100 / A_0$, where, A_0 is the initial absorbance and A_f is the final absorbance at 610 nm. The UV-Vis curves in Figure 7 indicate that even at the lowest concentration α-MnO_2-0.025% (*w/v*), there is at least 80% degradation. This demonstrates that the catalytic efficiency of these α-MnO_2 nanorods is comparable to that of MnO_2 nanoparticles synthesized using conventional procedures [32,33,36,41,47,80,81]. The reusability of the α-MnO_2 nanorods was also investigated by collecting and using the same powder sample for

up to four cycles. As shown in Figure S3b, the catalytic activity is not significantly altered by up to four cycles of degrading the IC dye.
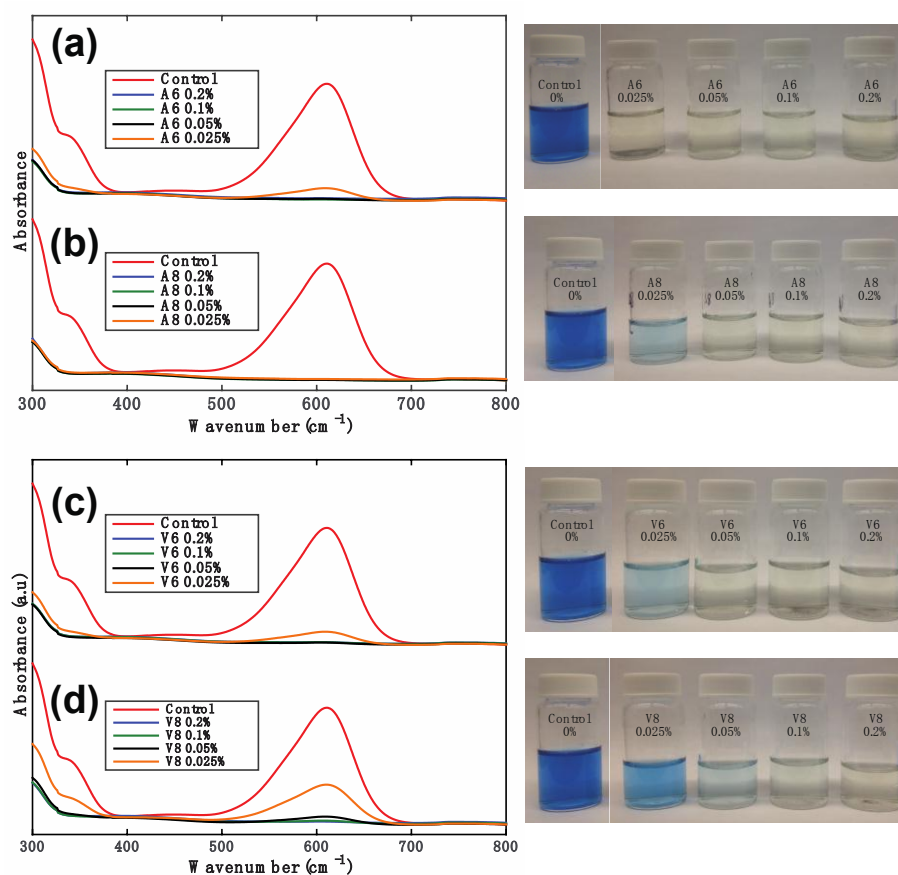

Figure 7. Ultraviolet-visible (UV-Vis) spectra of indigo carmine solutions after exposure to α-MnO_2 nanorods at various concentrations. (**a**,**b**) samples synthesized with the *Malus domestica* apple peels extract; (**c**,**d**) samples synthesized with the *Vitis vinifera* grape stems extract. The right hand side shows digital photographs of the color change of the specimens.

3. Materials and Methods

3.1. Materials

Vitis vinifera grape stems and *Malus domestica* apple peels (Cortland type), were obtained from a local market in Ithaca, NY, USA Potassium permanganate ($KMnO_4$), was purchased from Sigma-Aldrich (St. Louis, MO, USA) and used as received. Milli-Q water with a conductivity <18.2 MΩ·cm at 25 °C (Milli-Q Millipore filter system, Millipore Co., Bedford, MA, USA) was used.

3.2. Infusion Preparation

Vitis vinifera grape stems and *Malus domestica* apple peels (Cortland type), were thoroughly rinsed with MilliQ water and dried in an oven at 70 °C. The dried biomass was ground into powder and stored at room temperature. Ten grams of dry biomass powder was mixed in 100 mL of MilliQ water (solid weight content of 0.1 g powder per mL) and refluxed for 1 h at 70 °C. The suspension was filtered using a cotton fabric to remove the solid particles. The suspension was centrifuged at 10,000 rpm for 10 min and filtered through a 0.2 μm filter (Millipore, Bedford, MA, USA). The pH value of the infusions ranged between 3.7 and 4.0.

3.3. Nanoparticle Synthesis

Ten mL of a 0.1 M aqueous solution of $KMnO_4$ was added dropwise to 40 mL of the filtered infusions at 25 °C under continuous stirring. After 2 h, a black precipitate was observed, indicating the initial formation of manganese oxide nanoparticles. The precipitate was washed several times with DI water and centrifuged at 10,000 rpm for 15 min. The resulting powders were dried in an air oven at 80 °C for 24 h, calcinated using a 30 °C/min ramp up to the target temperature (600 °C, 800 °C), and kept at this temperature for 4 h.

3.4. Dye Degradation Experiments

The catalytic activity of the synthesized α-MnO_2 nanorods was assessed by dye degradation of aqueous solutions of indigo carmine (IC). Indigo carmine (5,5-indigodisulfonic acid sodium salt) is one of the oldest synthetic dyes known and is still one of the most used dyes in the textile industry [82]. The primary color-producing structure of indigoid dyes is a cross-conjugated system or H-chromophore, consisting of a single –C=C– double bond substituted by two NH donor groups and two CO acceptor groups [83]. The dye stock solution was prepared by dissolving 0.020 g of Indigo Carmine in 1000 mL of MilliQ water. Ten mL of the dye stock solution were placed in 20 mL vials, and the pH was adjusted to 2.5 using acetic acid. α-MnO_2 powders were added at different weight/volume percent concentrations (0.2%, 0.1%, 0.05%, 0.025%) to the pH adjusted vials. The vials were vortexed for 30 s and centrifuged at 10,000 rpm for 15 min. The recovered supernatant was analyzed, immediately after centrifugation, using a Perkin–Elmer Lambda 35 UV-Vis spectrophotometer. The absorption peak was set at 610 nm. The control sample consisted of 20 ppm of indigo carmine dye, at pH 2.5, without manganese oxide. The percentage of degradation was calculated using the ratio between the characteristic UV-Vis absorption band of indigo carmine in solution at λ = 610 nm before and after contact with the α-MnO_2 powder.

3.5. Characterization

The morphology of the α-MnO_2 powders was investigated using a field emission scanning electron microscope (FESEM) (LEO 1550) (Carl Zeiss, Oberkoehen, Germany) with an accelerating voltage of 5 kV. TEM images were collected on a FEI Tecnai T12 Spirit TEM (FEI, Hillsboro, OR, USA) with an acceleration voltage of 120 keV. Samples for FESEM and TEM imaging were drop casted onto carbon coated copper grids and left to dry at ambient conditions. The samples were further characterized using a Scintag X-ray Diffractometer (Scintag Inc., Cupertino, CA, USA) with Cu–Kα radiation (40 KV, 40 mA). The XRD patterns were recorded at room temperature with a step-size of 0.02° in the range of 10°–80°. Fourier transform infrared (FTIR) spectra of the samples were acquired using a Bruker Hyperion FTIR Spectrometer (Bruker Optics, Billerica, MA, USA) in potassium bromide (KBr) pellet transmission (KPT) mode. The KBr powders and the α-MnO_2 powders were dried overnight in a vacuum oven prior to pellet preparation. The ratio of the sample powders to KBr was 1 mg of sample to 300 mg of KBr. X-ray photoelectron spectroscopy (XPS) measurements were performed in a surface science instruments (SSI) model SSX0100 (Surface Science Instruments, Mountain View, CA, USA) with monochromatic aluminum K-α X-rays (1486.6 eV). The analysis of peak binding energy (BE) and deconvolution was performed using the CASAXPS software (Casa Software Ltd, Teignmouth, UK), in which a Shirley background subtraction was used, as well as 50:50 Gaussian:Lorentzian line widths. All XPS measurements were corrected for charging using the C 1 s peak position at 284.8 eV. A physical properties measurement system (PPMS), equipped with a vibrating sample magnetometer (VSM), by Quantum Design (San Diego, CA, USA), was used to collect zero-field-cooled (ZFC) and field-cooled (FC) magnetization curves from 5 K to 300 K in an applied field of 100 Oe. In addition, isothermal magnetizations and hysteresis loops were collected at 300 K and 5 K for the applied fields ranging from −7 kOe to 7 kOe. UV spectrophotometry spectra were collected on a Perkin Elmer Lambda 35 spectrometer. The phytochemicals in the extracts were identified by gas chromatography-mass

spectrometry (GC-MS). The GC-MS analysis was performed on an Agilent 6890 N gas chromatograph (Agilent Technologies, Santa Clara, CA, USA) equipped with an Agilent 7683 automatic liquid sampler coupled to an Agilent 5973 N mass selective detector. The extracts for phytochemical analysis were prepared using 25 mg/mL of biomass powder with high performance liquid chromatography (HPLC) grade alcohol. This mixture was stirred during 8 h, and the extracts were centrifuged and filtered through a 25-mm syringe filter. The mobile phase (Helium) was injected at a flow rate of 1.2 mL min^{-1}, at a pressure of 10 psi, and with an injector temperature of 270 °C. The other parameters were adjusted as follows: the temperature of the column was initiated at 50 °C and held for 5 min, then increased to 210 °C at a rate of 15 °C min^{-1}. Finally, the temperature was increased to 305 °C at a rate of 20 °C min^{-1} and held for 40 min. The samples were injected in the splitless mode and each injection was 5.0 μL. The MS detector was operated in full scan mode (35–600 amu). The retention times of each sample were compared to those reported in the national institute of standards and technology (NIST) mass spectral database. Figure S2 shows the GC-MS spectra of the extracts and a list of the constituents is provided in Tables S1 and S2.

4. Conclusions

We report a facile strategy to synthesize functional α-MnO$_2$ nanorods using natural extracts of apple peels and grape stems, follow by a sequential calcination process that induces an oriented attachment growth. We found evidence that the phytochemicals in the extracts act as both reducing and protecting agents, and during the calcination process enable the transformation of the stable nuclei into chemically ordered nanorods with preferential orientations. This facile synthetic strategy may provide a way to explore the formation of MnO$_2$ nanostructures with different crystal phases and morphologies. The reported synthesis method, based on the separation of nucleation and the subsequent growth processes, may serve as a strategy for the further investigation of crystal growth in anisotropic nanoparticles. The results also show that the nanorods, synthesized with natural extracts exhibit interesting catalytic properties including the efficient degradation of dyes. These high-crystalline α-MnO$_2$ nanorods represent a new platform for further studies of nanoscale phenomena as well as for applications such as water purification.

Author Contributions: L.S.B. synthesized and characterized the particles, analyzed the data, and wrote the paper. A.P.H. and J.P.H., supervised the study, analyzed the data, and contributed to the writing of the paper.

Conflicts of Interest: The authors declare no conflict of interest.

References

1.　Niu, W.; Xu, G. Crystallographic control of noble metal nanocrystals. *Nano Today* **2011**, *6*, 265–285. [CrossRef]

2.　Einarsrud, M.-A.; Grande, T. 1D oxide nanostructures from chemical solutions. *Chem. Soc. Rev.* **2014**, *43*, 2187–2199. [CrossRef] [PubMed]

3.　Guo, T.; Yao, M.-S.; Lin, Y.-H.; Nan, C.-W. A comprehensive review on synthesis methods for transition-metal oxide nanostructures. *CrystEngComm* **2015**, *17*, 3551–3585. [CrossRef]

4.　Xia, Y.; Xiong, Y.; Lim, B.; Skrabalak, S.E. Shape-controlled synthesis of metal nanocrystals: Simple chemistry meets complex physics? *Angew. Chem. Int. Ed.* **2009**, *48*, 60–103. [CrossRef] [PubMed]

5.　Zhang, Z.; Lu, M.; Xu, H.; Chin, W.-S. Shape-controlled synthesis of zinc oxide: A simple method for the preparation of metal oxide nanocrystals in non-aqueous medium. *Chemistry* **2007**, *13*, 632–638. [CrossRef] [PubMed]

6. Kojtari, A.; Ji, H.-F. Metal Organic Framework Micro/Nanopillars of Cu(BTC)·3H$_2$O and Zn(ADC)·DMSO. *Nanomaterials* **2015**, *5*, 565–576. [CrossRef] [PubMed]

7. Xue, X.; Penn, R.L.; Leite, E.R.; Huang, F.; Lin, Z. Crystal growth by oriented attachment: Kinetic models and control factors. *CrystEngComm* **2014**, *16*, 1419–1429. [CrossRef]

8. Welch, D.A.; Woehl, T.J.; Park, C.; Faller, R.; Evans, J.E.; Browning, N.D. Understanding the role of solvation forces on the preferential attachment of nanoparticles in liquid. *ACS Nano* **2016**, *10*, 181–187. [CrossRef] [PubMed]

9. Sau, T.K.; Rogach, A.L. Nonspherical noble metal nanoparticles: Colloid-chemical synthesis and morphology control. *Adv. Mater.* **2010**, *22*, 1781–1804. [CrossRef] [PubMed]

10. Tao, A.R.; Habas, S.; Yang, P. Shape control of colloidal metal nanocrystals. *Small* **2008**, *4*, 310–325. [CrossRef]

11. Anastas, P.T.; Warner, J.C. *Green Chemistry: Theory and Practice*; Oxford University Press: New York, NY, USA, 1998.

12. Virkutyte, J.; Varma, R.S. Environmentally friendly preparation of metal nanoparticles. *RSC Green Chem.* **2013**, *19*, 7–33.

13. Bhau, B.S.; Ghosh, S.; Puri, S.; Borah, B.; Sarmah, D.K.; Khan, R. Green synthesis of gold nanoparticles from the leaf extract of Nepenthes khasiana and antimicrobial assay. *Adv. Mater. Lett.* **2015**, *6*, 55–58. [CrossRef]

14. Vinod, V.T.P.; Saravanan, P.; Sreedhar, B.; Devi, D.K.; Sashidhar, R.B. A facile synthesis and characterization of Ag, Au and Pt nanoparticles using a natural hydrocolloid gum kondagogu (*Cochlospermum gossypium*). *Colloids Surf. B Biointerfaces* **2011**, *83*, 291–298. [CrossRef] [PubMed]

15. Mandal, M.; Kundu, S.; Ghosh, S.K.; Panigrahi, S.; Sau, T.K.; Yusuf, S.M.; Pal, T. Magnetite nanoparticles with tunable gold or silver shell. *J. Colloid Interface Sci.* **2005**, *286*, 187–194. [CrossRef] [PubMed]

16. Venkateswarlu, S.; Natesh Kumar, B.; Prathima, B.; Anitha, K.; Jyothi, N.V.V. A novel green synthesis of Fe$_3$O$_4$-Ag core shell recyclable nanoparticles using Vitis vinifera stem extract and its enhanced antibacterial performance. *Phys. B Condens. Matter* **2015**, *457*, 30–35. [CrossRef]

17. Saif, S.; Tahir, A.; Chen, Y. Green synthesis of iron nanoparticles and their environmental applications and implications. *Nanomaterials* **2016**, *6*, 209. [CrossRef] [PubMed]

18. Keihan, A.H.; Veisi, H.; Veasi, H. Green synthesis and characterization of spherical copper nanoparticles as organometallic antibacterial agent. *Appl. Organomet. Chem.* **2016**, 1–7. [CrossRef]

19. Saif, S.; Tahir, A.; Asim, T.; Chen, Y. Plant Mediated Green Synthesis of CuO Nanoparticles: Comparison of Toxicity of Engineered and Plant Mediated CuO Nanoparticles towards Daphnia magna. *Nanomaterials* **2016**, *6*, 205. [CrossRef] [PubMed]

20. Veisi, H.; Rostami, A.; Shirinbayan, M. Greener approach for synthesis of monodispersed palladium nanoparticles using aqueous extract of green tea and their catalytic activity for the Suzuki-Miyaura coupling reaction and the reduction of nitroarenes. *Appl. Organomet. Chem.* **2016**, 1–9. [CrossRef]

21. Rajakumar, G.; Rahuman, A.A.; Chung, I.M.; Kirthi, A.V.; Marimuthu, S.; Anbarasan, K. Antiplasmodial activity of eco-friendly synthesized palladium nanoparticles using Eclipta prostrata extract against Plasmodium berghei in Swiss albino mice. *Parasitol. Res.* **2015**, *114*, 1397–1406. [CrossRef] [PubMed]

22. Chung, I.; Rahuman, A.A.; Marimuthu, S.; Kirthi, A.V.; Anbarasan, K.; Rajakumar, G. An Investigation of the Cytotoxicity and Caspase-Mediated Apoptotic Effect of Green Synthesized Zinc Oxide Nanoparticles Using Eclipta prostrata on Human Liver Carcinoma Cells. *Nanomaterials* **2015**, *5*, 1317–1330. [CrossRef] [PubMed]

23. Raveendran, P.; Fu, J.; Wallen, S.L. Completely "Green" Synthesis and Stabilization of Metal Nanoparticles. *J. Am. Chem. Soc.* **2003**, *125*, 13940–13941. [CrossRef] [PubMed]

24. Ahmed, S.; Ahmad, M.; Swami, B.L.; Ikram, S. A review on plants extract mediated synthesis of silver nanoparticles for antimicrobial applications: A green expertise. *J. Adv. Res.* **2016**, *7*, 17–28. [CrossRef] [PubMed]

25. Gopinath, V.; MubarakAli, D.; Priyadarshini, S.; Priyadharsshini, N.M.; Thajuddin, N.; Velusamy, P. Biosynthesis of silver nanoparticles from Tribulus terrestris and its antimicrobial activity: A novel biological approach. *Colloids Surf. B Biointerfaces* **2012**, *96*, 69–74. [CrossRef] [PubMed]

26. Venkatesan, J.; Kim, S.-K.; Shim, M. Antimicrobial, Antioxidant, and Anticancer Activities of Biosynthesized Silver Nanoparticles Using Marine Algae Ecklonia cava. *Nanomaterials* **2016**, *6*, 235. [CrossRef] [PubMed]

27. Xia, Q.; Ma, Y.; Wang, J. Biosynthesis of Silver Nanoparticles Using Taxus yunnanensis Callus and Their Antibacterial Activity and Cytotoxicity in Human Cancer Cells. *Nanomaterials* **2016**, *6*, 160. [CrossRef] [PubMed]

28. Yan, D.; Zhang, H.; Chen, L.; Zhu, G.; Wang, Z.; Xu, H.; Yu, A. Supercapacitive properties of Mn_3O_4 nanoparticles bio-synthesized from banana peel extract. *RSC Adv.* **2014**, *1*, 23649–23652. [CrossRef]

29. Sinha, A.; Singh, V.N.; Mehta, B.R.; Khare, S.K. Synthesis and characterization of monodispersed orthorhombic manganese oxide nanoparticles produced by Bacillus sp. cells simultaneous to its bioremediation. *J. Hazard. Mater.* **2011**, *192*, 620–627. [CrossRef] [PubMed]

30. Sharma, J.K.; Srivastava, P.; Ameen, S.; Akhtar, M.S.; Singh, G. Azadirachta indica plant-assisted green synthesis of Mn_3O_4 nanoparticles: Excellent thermal catalytic performance and chemical sensing behavior. *J. Colloid Interface Sci.* **2016**, *472*, 220–228. [CrossRef] [PubMed]

31. Stoerzinger, K.A.; Risch, M.; Han, B.; Shao-Horn, Y. Recent Insights into Manganese Oxides in Catalyzing Oxygen Reduction Kinetics. *ACS Catal.* **2015**, *5*, 6021–6031. [CrossRef]

32. Tang, N.; Tian, X.; Yang, C.; Pi, Z.; Han, Q. Facile synthesis of α-MnO_2 nanorods for high-performance alkaline batteries. *J. Phys. Chem. Solids* **2010**, *71*, 258–262. [CrossRef]

33. Qu, Q.; Zhang, P.; Wang, B.; Chen, Y.; Tian, S.; Wu, Y.; Holze, R. Electrochemical performance of MnO_2 nanorods in neutral aqueous electrolytes as a cathode for asymmetric supercapacitors. *J. Phys. Chem. C* **2009**, *113*, 14020–14027. [CrossRef]

34. Tompsett, D.A.; Parker, S.C.; Islam, M.S. Surface properties of α-MnO_2: Relevance to catalytic and supercapacitor behaviour. *J. Mater. Chem. A* **2014**, *2*, 15509. [CrossRef]

35. Li, W.; Cui, X.; Zeng, R.; Du, G.; Sun, Z.; Zheng, R.; Ringer, S.P.; Dou, S.X. Performance modulation of α-MnO_2 nanowires by crystal facet engineering. *Sci. Rep.* **2015**, *5*, 8987. [CrossRef] [PubMed]

36. Jaganyi, D.; Altaf, M.; Wekesa, I. Synthesis and characterization of whisker-shaped MnO_2 nanostructure at room temperature. *Appl. Nanosci.* **2013**, *3*, 329–333. [CrossRef]

37. Tang, B.; Wang, G.; Zhuo, L.; Ge, J. Novel dandelion-like beta-manganese dioxide microstructures and their magnetic properties. *Nanotechnology* **2006**, *17*, 947–951. [CrossRef] [PubMed]

38. Chacón-Patiño, M.L.; Blanco-Tirado, C.; Hinestroza, J.P.; Combariza, M.Y. Biocomposite of nanostructured MnO_2 and fique fibers for efficient dye degradation. *Green Chem.* **2013**, *15*, 2920. [CrossRef]

39. Clarke, C.E.; Kielar, F.; Talbot, H.M.; Johnson, K.L. Oxidative decolorization of acid azo dyes by a mn oxide containing waste. *Environ. Sci. Technol.* **2010**, *44*, 1116–1122. [CrossRef] [PubMed]

40. Duan, L.; Sun, B.; Wei, M.; Luo, S.; Pan, F.; Xu, A.; Li, X. Catalytic degradation of Acid Orange 7 by manganese oxide octahedral molecular sieves with peroxymonosulfate under visible light irradiation. *J. Hazard. Mater.* **2015**, *285*, 356–365. [CrossRef] [PubMed]

41. Dang, T.; Cheney, M.A.; Qian, S.; Joo, S.W.; Min, B. A Novel Rapid One-Step Synthesis of Manganese Oxide Nanoparticles at Room Temperature Using Poly (dimethylsiloxane). *Ind. Eng. Chem. Res.* **2013**, *52*, 2750–2753. [CrossRef]

42. Najafpour, M.M.; Renger, G.; Hołyńska, M.; Moghaddam, A.N.; Aro, E.M.; Carpentier, R.; Nishihara, H.; Eaton-Rye, J.J.; Shen, J.R.; Allakhverdiev, S.I. Manganese Compounds as Water-Oxidizing Catalysts: From the Natural Water-Oxidizing Complex to Nanosized Manganese Oxide Structures. *Chem. Rev.* **2016**, *116*, 2886–2936. [CrossRef] [PubMed]

43. Fei, J.; Cui, Y.; Yan, X.; Qi, W.; Yang, Y.; Wang, K.; He, Q.; Li, J. Controlled preparation of MnO_2 hierarchical hollow nanostructures and their application in water treatment. *Adv. Mater.* **2008**, *20*, 452–456. [CrossRef]

44. Xiao, W.; Wang, D.; Lou, X.W. Shape-Controlled Synthesis of MnO_2 Nanostructures with Enhanced Electrocatalytic Activity for Oxygen Reduction. *J. Phys. Chem. C* **2010**, *114*, 1694–1700. [CrossRef]

45. Wang, X.; Li, Y. Selected-Control Hydrothermal Synthesis of α- and β-MnO_2 Single Crystal Nanowires. *J. Am. Chem. Soc.* **2002**, *124*, 2880–2881. [CrossRef] [PubMed]

46. He, X.; Wang, J.; Kloepsch, R.; Krueger, S.; Jia, H.; Liu, H.; Vortmann, B.; Li, J. Enhanced electrochemical performance in lithium ion batteries of a hollow spherical lithium-rich cathode material synthesized by a molten salt method. *Nano Res.* **2014**, *7*, 110–118. [CrossRef]

47. Wang, N.; Cao, X.; Lin, G.; Shihe, Y. λ-MnO_2 Nanodisks and Their Magnetic Properties. *Nanotechnology* **2007**, *18*, 475605. [CrossRef]

48. Kim, H.J.; Lee, J.B.; Kim, Y.-M.; Jung, M.-H.; Jagličić, Z.; Umek, P.; Dolinšek, J. Synthesis, structure and magnetic properties of β-MnO_2 nanorods. *Nanoscale Res. Lett.* **2007**, *2*, 81–86. [CrossRef]

49. Tseng, L.-T.; Lu, Y.; Fan, H.M.; Wang, Y.; Luo, X.; Liu, T.; Munroe, P.; Li, S.; Yi, J. Magnetic properties in α-MnO_2 doped with alkaline elements. *Sci. Rep.* **2015**, *5*, 1–8. [CrossRef] [PubMed]

50. Shafi, P.M.; Bose, A.C. Structural evolution of tetragonal MnO$_2$ and its electrochemical behavior. *AIP Conf. Proc.* **2016**, *1731*, 2–5.

51. Wu, Y.; Lu, Y.; Song, C.; Ma, Z.; Xing, S.; Gao, Y. A novel redox-precipitation method for the preparation of α-MnO$_2$ with a high surface Mn4+ concentration and its activity toward complete catalytic oxidation of o-xylene. *Catal. Today* **2013**, *201*, 32–39. [CrossRef]

52. Wu, Y.; Li, S.; Cao, Y.; Xing, S.; Ma, Z.; Gao, Y. Facile synthesis of mesoporous α-MnO2 nanorod with three-dimensional frameworks and its enhanced catalytic activity for VOCs removal. *Mater. Lett.* **2013**, *97*, 1–3. [CrossRef]

53. Wang, H.; Lu, Z.; Qian, D.; Li, Y.; Zhang, W. Single-crystal α-MnO2 nanorods: Synthesis and electrochemical properties. *Nanotechnology* **2007**, *18*, 115616. [CrossRef]

54. Momma, K.; Izumi, F. VESTA 3 for three-dimensional visualization of crystal, volumetric and morphology data. *J. Appl. Crystallogr.* **2011**, *44*, 1272–1276. [CrossRef]

55. Sun, M.; Lan, B.; Lin, T.; Cheng, G.; Ye, F.; Yu, L.; Cheng, X.; Zheng, X. Controlled synthesis of nanostructured manganese oxide: crystalline evolution and catalytic activities. *CrystEngComm* **2013**, *15*, 7010. [CrossRef]

56. Post, J.E. Manganese oxide minerals: Crystal structures and economic and environmental significance. *Proc. Natl. Acad. Sci. USA* **1999**, *96*, 3447–3454. [CrossRef] [PubMed]

57. Cheng, S.; Yang, L.; Chen, D.; Ji, X.; Jiang, Z.-J.; Ding, D.; Liu, M. Phase evolution of an alpha MnO$_2$-based electrode for pseudo-capacitors probed by in operando Raman spectroscopy. *Nano Energy* **2014**, *9*, 161–167. [CrossRef]

58. Stuart, B.H. *Infrared Spectroscopy: Fundamentals and Applications*; John Wiley and Sons: Hoboken, NJ, USA, 2004.

59. Chertihin, G.V.; Andrews, L. Reactions of Laser-Ablated Manganese Atoms with Dioxygen. Infrared Spectra of MnO, OMnO, Mn(O)$_2$, (MnO)$_2$, and Higher Oxide Complexes in Solid Argon. *J. Phys. Chem. A* **1997**, *101*, 8547–8553. [CrossRef]

60. Di Castro, V.; Polzonetti, G. XPS study of MnO oxidation. *J. Electron Spectros. Relat. Phenom.* **1989**, *48*, 117–123. [CrossRef]

61. Nesbitt, H.W.; Banerjee, D. Interpretation of XPS Mn(2P) spectra of Mn oxyhydroxides and constraints on the mechanism of MnO$_2$ precipitation. *Am. Mineral.* **1998**, *83*, 305–315. [CrossRef]

62. Biesinger, M.C.; Payne, B.P.; Grosvenor, A.P.; Lau, L.W.M.; Gerson, A.R.; Smart, R.S.C. Resolving surface chemical states in XPS analysis of first row transition metals, oxides and hydroxides: Cr, Mn, Fe, Co and Ni. *Appl. Surf. Sci.* **2011**, *257*, 2717–2730. [CrossRef]

63. Naumkin, A.V.; Kraut-Vass, A.; Gaarenstroom, S.W.; Powell, C.J. NIST X-ray Photoelectron Spectroscopy Database. Available online: http://srdata.nist.gov/xps/Default.aspx (accessed on July 2016).

64. Gupta, R.P.; Sen, S.K. Calculation of multiplet structure of core p-vacancy levels. *Phys. Rev. B* **1974**, *10*, 71–79. [CrossRef]

65. Foord, J.S.; Jackman, R.B.; Allen, G.C. An X-ray photoelectron spectroscopic investigation of the oxidation of manganese. *Philos. Mag. A* **1984**, *49*, 657–663. [CrossRef]

66. Giri, S.; Patra, M.; Majumdar, S. Exchange bias effect in alloys and compounds. *J. Phys. Condens. Matter* **2011**, *23*, 73201. [CrossRef] [PubMed]

67. Yoshimori, A. A New Type of Antiferromagnetic Structure in the Rutile Type Crystal. *J. Phys. Soc. Japan* **1959**, *14*, 807–821. [CrossRef]

68. Zheng, X.G.; Xu, C.N.; Nishikubo, K.; Nishiyama, K.; Higemoto, W.; Moon, W.J.; Tanaka, E.; Otabe, E.S. Finite-size effect on Néel temperature in antiferromagnetic nanoparticles. *Phys. Rev. B Condens. Matter Mater. Phys.* **2005**, *72*, 1–8. [CrossRef]

69. Zhang, T.; Zhou, T.F.; Qian, T.; Li, X.G. Particle size effects on interplay between charge ordering and magnetic properties in nanosized La$_{0.25}$Ca$_{0.75}$MnO$_3$. *Phys. Rev. B* **2007**, *76*, 174415. [CrossRef]

70. Umek, P.; Zorko, A.; Arčon, D. Magnetic Properties of Transition-Metal Oxides: From Bulk to Nano. *ChemInform* **2013**, *42*, 2–4.

71. Luo, J.; Zhu, H.T.; Zhang, F.; Liang, J.K.; Rao, G.H.; Li, J.B.; Du, Z.M. Spin-glasslike behavior of K+ containing α-MnO$_2$ nanotubes. *J. Appl. Phys.* **2016**, *93925*, 2–7. [CrossRef]

72. Polleux, J.; Pinna, N.; Antonietti, M.; Niederberger, M. Ligand-Directed Assembly of Preformed Titania Nanocrystals into Highly Anisotropic Nanostructures. *Adv. Mater.* **2004**, *16*, 2002–2005. [CrossRef]

73. Tang, Z.; Kotov, N.A.; Giersig, M. Spontaneous Organization of Single CdTe Nanoparticles into Luminescent Nanowires. *Science.* **2002**, *297*, 237–241. [CrossRef] [PubMed]

74. Aromal, S.A.; Philip, D. Green synthesis of gold nanoparticles using Trigonella foenum-graecum and its size-dependent catalytic activity. *Spectrochim. Acta Part A Mol. Biomol. Spectrosc.* **2012**, *97*, 1–5. [CrossRef] [PubMed]

75. Kharissova, O.V.; Rasika-Dias, H.V.; Kharisov, B.I.; Olvera-Perez, B.; Jimenez-Perez, V.M. The greener synthesis of nanoparticles. *Trends Biotechnol.* **2013**, *31*, 240–248. [CrossRef] [PubMed]

76. Kuppusamy, P.; Yusoff, M.M.; Maniam, G.P. Biosynthesis of metallic nanoparticles using plant derivatives and their new avenues in pharmacological applications—An updated report. *Saudi Pharm. J.* **2016**, *24*, 473–484. [CrossRef] [PubMed]

77. Makarov, V.V.; Love, A.J.; Sinitsyna, O.V.; Makarova, S.S.; Yaminsky, I.V. "Green" Nanotechnologies: Synthesis of Metal Nanoparticles Using Plants. *ActaNaturae* **2014**, *6*, 35–44.

78. Kumar, K.; Amutha, R.; Arumugam, P.; Berchmans, S. Synthesis of Gold Nanoparticles: An Ecofriendly Approach Using Hansenula anomala. *ACS Appl. Mater. Interfaces* **2011**, *3*, 1418–1425.

79. Abdel-aal, E.I.; Haroon, A.M.; Mofeed, J. Successive solvent extraction and GC-MS analysis for the evaluation of the phytochemical constituents of the filamentous green alga Spirogyra longata. *Egypt. J. Aquat. Res.* **2015**, *41*, 233–246. [CrossRef]

80. Boppana, V.B.R.; Jiao, F. Nanostructured MnO_2: An efficient and robust water oxidation catalyst. *Chem. Commun. (Camb.)* **2011**, *47*, 8973–8975. [CrossRef] [PubMed]

81. Yuan, A.; Wang, X.; Wang, Y.; Hu, J. Textural and capacitive characteristics of MnO_2 nanocrystals derived from a novel solid-reaction route. *Electrochim. Acta* **2009**, *54*, 1021–1026. [CrossRef]

82. De Keijzer, M.; Van Bommel, M.R.; Keijzer, R.H.-d.; Knaller, R.; Oberhumer, E. Indigo carmine: Understanding a problematic blue dye. In Proceedings of the Decorative: Conservation and the Applied Arts. IIC Congress, Vienna, Austria, 10–14 September 2012; pp. 87–95.

83. Dähne, S.; Leupold, D. Coupling principles in organic dyes. *Angew. Chem. Int.* **1966**, *5*, 984–993. [CrossRef]